

# Carbon Backsputter Mitigation with a Retarding Beam Dump

IEPC-2024-504

*Presented at the 38th International Electric Propulsion Conference, Toulouse, France  
June 23-28, 2024*

Braden Oh,\* William Hurley,<sup>†</sup> Grace Zoppi,<sup>†</sup> Christopher May,<sup>‡</sup> Collin Whittaker,<sup>†</sup> and Benjamin Jorns<sup>§</sup>  
*Plasmadynamics and Electric Propulsion Laboratory, University of Michigan, Ann Arbor, MI, 48109*

The problem of backsputter, in which facility material sputtered by an ion beam returns to coat the source, impedes qualification testing by obscuring erosion of electric propulsion thruster components. This study demonstrates how electrostatic deceleration of ions prior to striking a beam dump may be used to reduce backsputter rates. A ‘beam catcher’ comprised of a positively biased graphite plate with a transverse magnetic field is tested. The magnetic field enables high decelerating potentials to be applied to the beam dump while minimally affecting thruster performance. A  $1.3 \times 0.66$  m prototype of this device was tested in the far-field plume of a 4.5 kW Hall effect thruster from biases of 0 V to 200 V and maximum magnetic field strengths from 0 G to 200 G. Measurements were made of the net backsputter rate at the thruster plane and of thruster operating metrics including the beam potential and shape of the far-field plume, the thrust, and the anode current oscillation spectrum. It was shown that the far-field plume potential and thrust levels do not vary within uncertainty at biases up to 150 V and that anode current oscillation power spectrum maxima occur at identical frequencies. Plume divergence appears to increase with applied bias potential. Backsputter rates are found to vary from  $2.91 \mu\text{m}/\text{kHr}$  for an unbiased beam dump to  $-1.99 \mu\text{m}/\text{kHr}$  for a 150 V biased plate. The negative backsputter rates indicate an erosion process believed to be caused by ions generated via charge exchange near the plate being launched back at the thruster by the beam dump bias. The implications of these findings and strategies for mitigating ion backstreaming are discussed in the context of establishing novel boundary conditions for next-generation propulsion system testing.

## I. Introduction

THE problem of backsputter, in which facility material eroded by an ion beam returns to coat the source, poses a challenge to qualification testing of long lifetime thrusters. The high specific impulse and low thrust of electric propulsion thrusters necessitate long duration missions, and thus they must be qualified in ground vacuum chambers for thousands of hours of operation. A primary goal of these tests is to detect erosion of critical components, which is a major life-limiting factor for electric propulsion thrusters (e.g., pole cover erosion in magnetically shielded Hall thrusters<sup>1–4</sup> or accelerator grid erosion in gridded ion thrusters<sup>5</sup>). Erosion worsens at higher powers as thruster current densities and/or beam energies increase,<sup>6–8</sup> underscoring the need to accurately measure erosion in contemporary electric rockets.

The problem of backsputter is that it obscures this detection and thereby threatens our ability to accurately measure thruster lifetime. Recent wear tests of the 12.5kW HERMeS and AEPS Hall effect thrusters and the 6.9kW NEXT ion thruster exhibited deposition of backsputtered carbon from graphite beam dumps onto the thruster surfaces exceeding the erosion rate.<sup>4,5,9</sup> It was also noted in these tests that beyond confounding erosion measurements, backsputter buildup impacted thruster performance,<sup>5</sup> altered component thermal emittance,<sup>10</sup> and induced shorting events.<sup>3</sup>

---

\*Ph.D. Precandidate

<sup>†</sup>Ph.D. Candidate

<sup>‡</sup>Undergraduate Researcher

<sup>§</sup>Associate Professor

To date, backscatter mitigation has largely been ignored for unshielded Hall thrusters (which erode rapidly) or been addressed by computational modeling for gridded ion thrusters and shielded Hall thrusters<sup>11,12</sup> (for which backscatter is non-negligible). However, this approach will likely become problematic as backscatter rates for contemporary thrusters with larger throughputs dominate the erosion process.<sup>7</sup> This makes model-based or *a posteriori* experimental deconvolution of backscatter and erosion rates impractical or impossible. Hence, for moderate and high-power testing it is increasingly desirable to find a way to mitigate backscatter at the facility level.

The effective goal is to mitigate the amount of material sputtered by ion beams with energies of 100-300 eV typical for Hall thrusters and 1-3 keV for ion thrusters. One novel approach for reducing backscatter at a facility level is using volumetrically complex materials (VCMs) to “catch” sputtered particles before they can escape. VCMs have shown some initial promise in reducing sputter yield,<sup>13</sup> but it is presently unclear whether VCMs can be scaled to large sizes or continue to exhibit low sputter yield during long-duration tests.

Another approach is to electrostatically decelerate ions to below the sputtering threshold of the beam dump positive biasing it relative to the beam. However, only a bias potential of  $\sim 30$  V can be applied with effect; beyond this bias level, the beam dump draws enough electrons from the main plasma beam to cause the potential of the main beam to rise accordingly.<sup>14</sup> Eventually, a constant potential difference between the plasma and beam dump is reached.<sup>14,15</sup> The impact of reaching this constant potential difference is an inability to further reduce ion energy by raising retarding potential alone.

To overcome this challenge, we hypothesized in recent work that reducing electron current to the beam dump would enable the near-field plasma potential to remain low even as the plate potential increases.<sup>16,17</sup> This would allow effective retarding potentials  $\gg 10\text{-}20$ V to be achieved. In Ref. 17, we applied a magnetic field transverse to a graphite bias plate to reduce electron mobility to the plate. Placed in the near field of a Hall thruster plume, this prototype beam catcher reduced backscatter by 20-38%, but it was limited to only  $\sim 40\text{-}50$ V retarding potential.<sup>17</sup> Attempts to actively bias the plate further caused an immediate rise in the cathode-to-ground voltage. A second prototype tested in the far field of a gridded ion thruster showed that applying sufficiently high bias voltages could completely eliminate backscatter, but may cause high-energy ions to be reflected at the thruster.<sup>16</sup> These prior studies are a positive proof of concept for the beam catcher, but they were conducted at a limited number of operating conditions and without detailed evaluation of the beam catcher’s impact on thruster performance. The beam catcher’s impact on the thrust plume and discharge characteristics, how significantly ion reflection may impact backscatter measurements, and whether scaling up the size of the beam catcher varies these effects remain to be characterized. The need is therefore apparent for a parametric study of beam catcher performance and thruster plume and current responses at a size, configuration, and power scale representative of contemporary thrusters.

In this paper, we test multiple configurations of the retarding beam catcher at representative operating conditions for a Hall effect thruster. In Section II, we review the retarding beam catcher concept and its theoretical foundation. In Section III, we explain our design for the beam catcher, the test setup, and the facility configuration. In Section IV we describe in detail the diagnostic tools and techniques we employ. In Section V we present the results of the experiment. In Section VII we discuss the implications of our findings in the context of the theory of operation of the beam catcher and modifications to improve operation.

## II. Theory

In this section, we overview the principle of operation and theory of the beam catcher concept. We first motivate the need to reduce ion energy. We then highlight the shortcoming of attempting to retard ion motion with a purely electric field. We conclude with a 0D first-principles analysis of how the introduction of a crossed magnetic field can address this shortcoming and improve the beam dump efficacy.

### A. Principle of operation

Conventional beam dumps consist of flat conducting plates placed downstream of a thruster ion beam.<sup>18</sup> When bombarded by high-energy ions, these plates are sputtered, releasing ejecta that recondense elsewhere in the facility (i.e., backscatter). Correspondingly, beam dumps are typically made of a low sputter yield material (e.g. graphite) to limit backscatter, though not to negligible levels. To further mitigate beam dump sputtering, our approach is to electrostatically decelerate the beam ions prior to striking the beam dump.

Figure 1 shows how the sputter yield of graphite varies with xenon ion energy.<sup>19</sup> The nonlinearity of the sputter curve means a modest reduction in ion energy causes a disproportionate reduction in sputter yield. Considering a typical Hall thruster ion beam energy of 300 eV ions,<sup>7</sup> a reduction of beam energy by 50% yields a backscatter reduction of approximately 84%, as shown in Fig. 1.

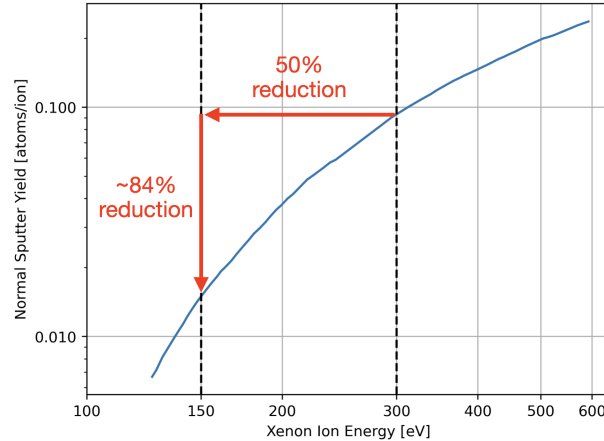


Figure 1. Sputter curve for graphite oriented normal to a xenon ion beam as reported by Williams et al.<sup>19</sup> The vertical lines at 300 eV and 150 eV represent the energy of the ion beam and the maximum decelerating voltage used in this study, respectively.

The most basic configuration for such a decelerating beam dump consists of a flat plate normal to the incident ion beam. A potential bias applied to the plate establishes an electric field perpendicular to the surface and thereby retards incoming ions. Fig. 2a illustrates the results of this approach for a realistic thruster test configuration in which the system is isolated from facility ground. With higher biases the beam

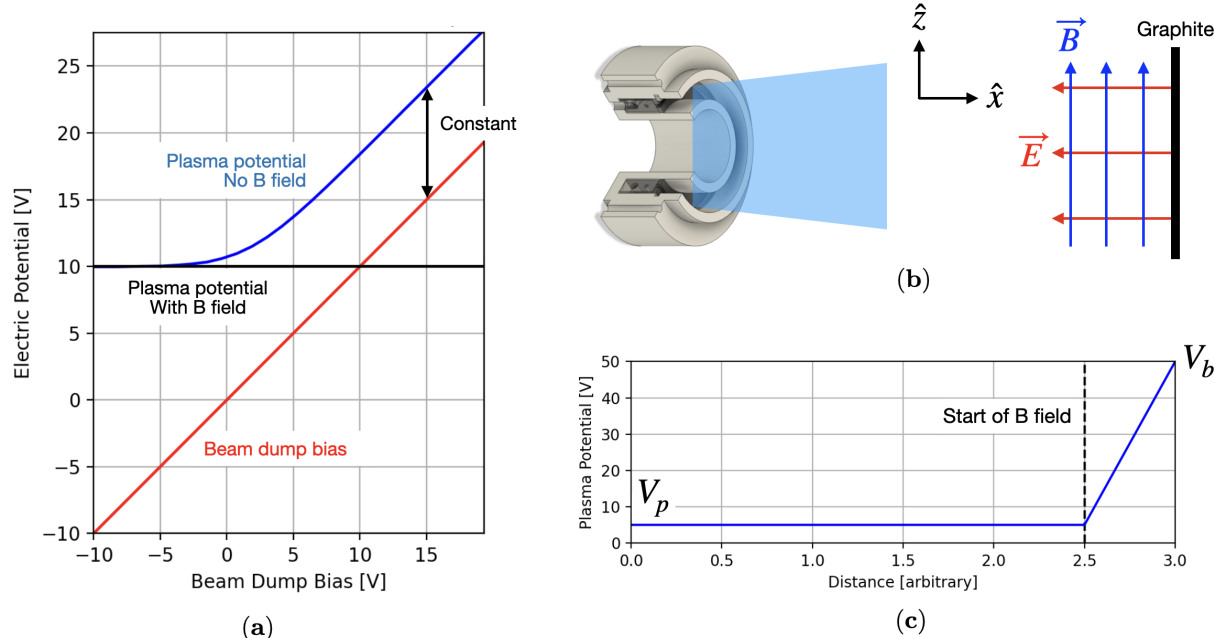


Figure 2. Notional illustrations of (a) plasma potential vs. beam dump bias without a magnetic field (blue) and with a magnetic field (black), (b) the beam catcher field geometry, and (c) the plasma potential as a function of distance (with a magnetic field). In (c)  $V_p$  and  $V_b$  represent plasma plume potential and plate bias potential, respectively.

dump draws electron current from the main plasma beam. The thruster can only source a finite number of ions, so as the beam dump draws electrons from the beam, the beam potential rises to maintain parity between the electron and ion currents. Eventually, the beam potential rise matches the retarding potential rise and a constant potential difference between the plasma and beam dump is reached.<sup>15</sup> In practice, this corresponding potential rise occurs before the beam dump bias exceeds the plasma potential, and a constant *accelerating* potential is reached, as illustrated in Fig. 2a.

To achieve larger ion energy reductions, this parasitic electron current to the beam dump must be reduced. This enables the near-field plasma potential to remain low even as the beam dump bias increases, allowing large effective retarding potentials to be achieved. Our approach to impeding the electron current (Fig. 2b) mirrors a conventional Hall thruster: we establish a magnetic field transverse to the electric field (parallel to the surface) to impede electron current to the plate. This increases the potential drop from the beam to plate for a given electron current, thereby allowing the beam dump to hold higher voltages without affecting the beam potential. Fig. 2c notionally illustrates the spatial variation in beam potential drop in this configuration, showing the ability to effectively isolate the plasma potential from the beam dump.

## B. Governing equations

In order to illustrate the behavior of the beam catcher and the influence of magnetic field, we motivate here a simplified 0D model for its response to the near field plasma, i.e. an expression that relates plate voltage to collected current. We first express the current collected by the plate,  $I_c$ , as a sum over the incident ion and electron fluxes:

$$I_c = A(j_{e,plate} + j_{i,plate}) \quad (1)$$

where  $A$  is the area of the plate, and  $j_{e,plate}$  and  $j_{i,plate}$  represent the electron and ion current densities, respectively, at the edge of the plate sheath. To evaluate this expression, we must obtain expressions for these current densities in terms of the plate voltage. For purposes of this derivation, we make a distinction between the ion current density at the sheath edge of the plate (denoted with the subscript “plate”) and in the quasineutral thruster plume (denoted as  $j_i$ ). We note here the following derivation is a generalization of the theory presented in our prior work.<sup>16,17</sup>

### 1. Electron Current Density

To derive an expression for electron current density, we begin from the electron fluid momentum equation,

$$m_e n_e \frac{d\vec{u}_e}{dt} = n_e q (\vec{E} + \vec{u}_e \times \vec{B}) - \nabla \cdot \bar{\vec{P}}_e - m_e n_e \nu (\vec{u}_e - \vec{u}_i) \quad (2)$$

where  $m_e$  is the electron mass,  $n_e$  is the electron number density,  $\vec{u}_e$  is the electron velocity vector,  $q$  is the fundamental charge,  $\vec{E}$  is an applied electric field,  $\vec{B}$  is an applied magnetic field,  $\bar{\vec{P}}_e$  is the electron pressure tensor,  $\nu$  is the total electron collision frequency, and  $\vec{u}_i$  is the ion velocity. We apply the fluid equation to the magnetic field region of our beam catcher by the following assumptions:

- **Cold electrons:** electron pressure scales with electron temperature  $P_e = n_e k T_e$ , hence for electron temperatures significantly below the applied electric potential, the electron pressure is negligible compared to electrostatic acceleration. This will be true for applied electric potentials at (or above) order  $10^1$  as far field plume electron temperatures are known to be  $\sim 1\text{-}3$  eV.<sup>7</sup>
- **Neglect transverse velocity:** Ions are assumed to be unmagnetized with velocity normal to the plate. As such, in the Hall direction given by  $\vec{E} \times \vec{B}$  (parallel to the plate as illustrated in Fig. 2b),  $\vec{u}_e \gg \vec{u}_i$ .
- **Inertialess electrons:** the acceleration term is negligible in magnitude when compared to the collisional and magnetic terms. This is a standard approximation for deriving the generalized Ohm’s law.<sup>20</sup>
- **Electron collisions follow Bohm scaling:** We assume the electron collision frequency follows a Bohm scaling,  $\nu = \alpha \omega_e$ , where  $\alpha$  is a scaling coefficient. This follows findings by Thompson et al.<sup>16</sup>

These assumptions simplify the momentum fluid equation (Eq. 2) to a form of the generalized Ohm's law:

$$mn_e\nu\vec{u}_e = qn_e\vec{E} + qn_e(\vec{u}_e \times \vec{B}). \quad (3)$$

This equation governs the relationship between the applied electric and magnetic fields and the resulting current. To resolve the electron current normal to the plate, we assume that the electric field is purely perpendicular to the plate,  $\vec{E} = E_x\hat{x}$ , and that the magnetic field is purely tangent to the plate,  $\vec{B} = B_z$ , as depicted in Fig. 2b. Solving Eq. 3 in the  $\hat{x}$  direction under these assumptions yields

$$j_{e,\text{plate}} = E_x \frac{q^2 n_e}{m_e} \frac{\nu}{\omega_e^2 + \nu^2}, \quad (4)$$

where  $\omega_e = qB/m_e$  denotes the electron cyclotron frequency.

To relate this current density to the plate bias and plasma potential, we further approximate the potential drop across the magnetic field region as decreasing linearly,  $E_x = (V_b - V_p)/L$ , where  $V_b$  is the beam dump bias voltage referenced with respect to facility ground,  $V_p$  is the beam plasma potential referenced with respect to ground, and  $L$  is the characteristic length of the magnetic field region. Hence,

$$j_{e,\text{plate}} = -\frac{(V_b - V_p)}{L} \frac{q^2 n_e}{m_e} \frac{\nu}{\omega_e^2 + \nu^2}. \quad (5)$$

This result demonstrates that electron current density to the plate increases with applied bias potential, as matches intuition. It also demonstrates that increasing magnetic field strength (increasing  $\omega_e$ ) drives higher impedance in the circuit and therefore reduces electron current density to the plate. This is the key enabling feature of the beam catcher—we exploit this magnetically driven impedance to choke the electron current to the plate. Applying a sufficiently strong magnetic field, therefore, allows us to hold electron current to the plate constant even in the presence of large plate biases. This circumvents the problem with the electric field-only configuration (illustrated in Fig. 2a) in which the plasma beam potential would otherwise be forced to follow the beam dump bias (Fig. 2a).

## 2. Ion Current Density

To find the ion current density at the plate, we evaluate the first moment of the ion velocity distribution,

$$j_{i,\text{plate}} = qn_i \int_{v_{\min}}^{\infty} v f_i(v) dv, \quad (6)$$

where  $n_i$  denotes the ion number density in the plume upstream of the magnetic field,  $f_i(v)$  is the ion velocity distribution function at this location, and  $v_{\min}$  is the minimum velocity an ion needs in order to cross the plume-plate potential barrier,

$$v_{\min} = \sqrt{\frac{2q}{m_i}(V_b - V_p)}, \quad (7)$$

where  $m_i$  represents the ion mass. We consider the incoming ions to be represented approximately by a drifting Maxwellian distribution:

$$f_i(v) = \left( \frac{m_i}{2\pi q T_i} \right)^{1/2} \exp \left( -\frac{m_i(v - v_p)^2}{2q T_i} \right), \quad (8)$$

where  $v_p$  denotes the average speed of ion beam in the plume and  $T_i$  denotes the ion temperature in eV. We can perform the integral in Eq. 6 using a change of variable from velocity to potential to arrive at the result,

$$j_{i,\text{plate}} = \frac{q^2 n_i}{m_i} \left( \frac{m_i}{2\pi q T_i} \right)^{1/2} \left[ \sqrt{\pi T_i V_{\text{acc}}} - \sqrt{\pi T_i V_{\text{acc}}} \operatorname{erf} \left( \frac{\sqrt{V_b} - \sqrt{V_{\text{acc}}}}{\sqrt{T_i}} \right) + T_i \exp \left( \frac{-(\sqrt{V_b} - \sqrt{V_{\text{acc}}})^2}{T_i} \right) \right], \quad (9)$$

where the bulk plume velocity is re-expressed in terms of the accelerating beam voltage  $v_p = \sqrt{2qV_{\text{acc}}/m_i}$ —neglecting multiply charged ions and assuming a monoenergetic beam—and the plume potential was

taken to be close to facility ground,  $V_p \sim 0$ . This latter assumption is borne out by previous experimental measurements of the far-field plume potential.<sup>7</sup>

For comparison, we also can find ion current density from the plume before it enters the magnetic field region,  $j_i$ . We arrive at this result by taking the first moment of the ion distribution function with a lower limit of 0 to capture all ions moving in the direction of the plate:

$$j_i = \frac{q^2 n_i}{m_i} \left( \frac{m_i}{2\pi q T_i} \right)^{1/2} \left[ \sqrt{\pi T_i V_{\text{acc}}} + \sqrt{\pi T_i V_{\text{acc}}} \operatorname{erf} \left( \sqrt{\frac{V_{\text{acc}}}{T_i}} \right) + T_i \exp \left( -\frac{V_{\text{acc}}}{T_i} \right) \right]. \quad (10)$$

We subsequently can use Eq. 10 to eliminate density in Eq. 9 to find:

$$j_{i,\text{plate}} = j_i \frac{\left[ 1 - \operatorname{erf} \left( \frac{\sqrt{V_b} - \sqrt{V_{\text{acc}}}}{\sqrt{T_i}} \right) + \sqrt{\frac{T_i}{\pi V_{\text{acc}}}} \exp \left( \frac{-(\sqrt{V_b} - \sqrt{V_{\text{acc}}})^2}{T_i} \right) \right]}{\left[ 1 + \operatorname{erf} \left( \sqrt{\frac{V_{\text{acc}}}{T_i}} \right) + \sqrt{\frac{T_i}{\pi V_{\text{acc}}}} \exp \left( -\frac{V_{\text{acc}}}{T_i} \right) \right]}. \quad (11)$$

For  $V_{\text{acc}}$  of order  $10^2$  V and  $T_i$  of order  $10^0$  V, we can make the approximation  $V_b \gg T_i$  (typical for the H9 operating at 15A on krypton<sup>7</sup>). This allows us to simplify the result, keeping only leading terms to find

$$j_{i,\text{plate}} = j_i \frac{1}{2} \left[ 1 - \operatorname{erf} \left( \frac{\sqrt{V_b} - \sqrt{V_{\text{acc}}}}{\sqrt{T_i}} \right) \right]. \quad (12)$$

This expression describes the ion current density at the plate as a fraction of the ion current density immediately outside of the ion deceleration region (i.e. beyond the beam catcher's magnetic field), which we take to be a known quantity (e.g., measured with a Faraday probe). In the limit where the beam catcher bias is zero, we recover the full current,  $j_i$ . In the case  $V_b = V_{\text{acc}}$ , we recover half of  $j_i$ , which is consistent with the assumption of the incoming ions having a Maxwellian distribution centered at  $V_{\text{acc}}$ . In the limit where  $V_b \gg V_{\text{acc}}$ , the plate ion current is driven to zero.

### 3. Total Plate Current

We now substitute our expressions for  $j_{i,\text{plate}}$  (Eq. 12) and  $j_{e,\text{plate}}$  (Eq. 5) back into Eq. 1 to find

$$I_c = A \left( -\frac{V_b}{L} \frac{q^2 n_e}{m_e} \frac{\nu}{\omega_e^2 + \nu^2} + j_i \frac{1}{2} \left[ 1 - \operatorname{erf} \left( \frac{\sqrt{V_b} - \sqrt{V_{\text{acc}}}}{\sqrt{T_i}} \right) \right] \right). \quad (13)$$

Here,  $n_e$  represents the number density of electrons at the plate sheath edge. To estimate this quantity, we invoke quasineutrality and scale the number density immediately outside of the retarding region via the zeroth moment of the ion velocity distribution,

$$n_e = \frac{j_i}{q \bar{v}_i} \int_{v_{\min}}^{\infty} f_i(v) dv, \quad (14)$$

where the average (unretarded) ion velocity is given by the accelerating potential,  $\bar{v}_i = \sqrt{2qV_{\text{acc}}/m}$ , assuming the plume potential  $V_p \sim 0$ . We perform this integral using the aforementioned change of variable to arrive at the result,

$$n_e = \frac{j_i}{2q} \sqrt{\frac{m_i}{2q}} \left[ 1 - \operatorname{erf} \left( \frac{\sqrt{V_b} - \sqrt{V_{\text{acc}}}}{\sqrt{T_i}} \right) \right] \frac{1}{\sqrt{V_{\text{acc}} - V_b}}. \quad (15)$$

Substituting into Eq. 13, we find a final expression for plate current (in front of the plate sheath),

$$I_c = \frac{A j_i}{2} \left[ 1 - \operatorname{erf} \left( \frac{\sqrt{V_b} - \sqrt{V_{\text{acc}}}}{\sqrt{T_i}} \right) \right] \left( 1 - \sqrt{\frac{m_i}{2q}} \frac{1}{\sqrt{V_{\text{acc}} - V_b}} \frac{q V_b \nu}{L m_e (\omega_e^2 + \nu^2)} \right). \quad (16)$$

As shown in Eq. 13, the total collected plate current is comprised of an ion contribution and an electron contribution. The comparative magnitude of these contributions determines whether the total collected current shown in Eq. 16 is net positive or negative. In the practical operating regime of this device,  $V_b$  is larger than the plasma potential and lower than the accelerating potential, making the electron current dominant ( $I_c < 0$ ). The electron current increases with bias voltage and decreases with magnetic field strength. We ultimately are able to regress this expression in later sections from direct experimental measurements of the beam catcher current, in which we treat the collision frequency,  $\nu$ , and the deceleration region length,  $L$ , as free parameters.

### C. Parametric results

Armed with the theoretical scaling law from the previous section, we can motivate key drivers for the performance of a beam catcher parametrically. To illustrate this, we examine the impact of magnetic field on the achievable plate bias voltage. We show this result in Fig. 3 where we have used model parameter values broadly consistent with those of our study, which are described in detail in Sections III and V. This result shows that the bias voltage required to draw a steady amount of beam current on the plate increases with magnetic field strength. We note that the "plate current" in Fig. 3 (and hereafter in the paper) is the current supplied by a biasing power supply to the bias plate, which has the same magnitude but opposite sign of the collected current of Eq. 16.

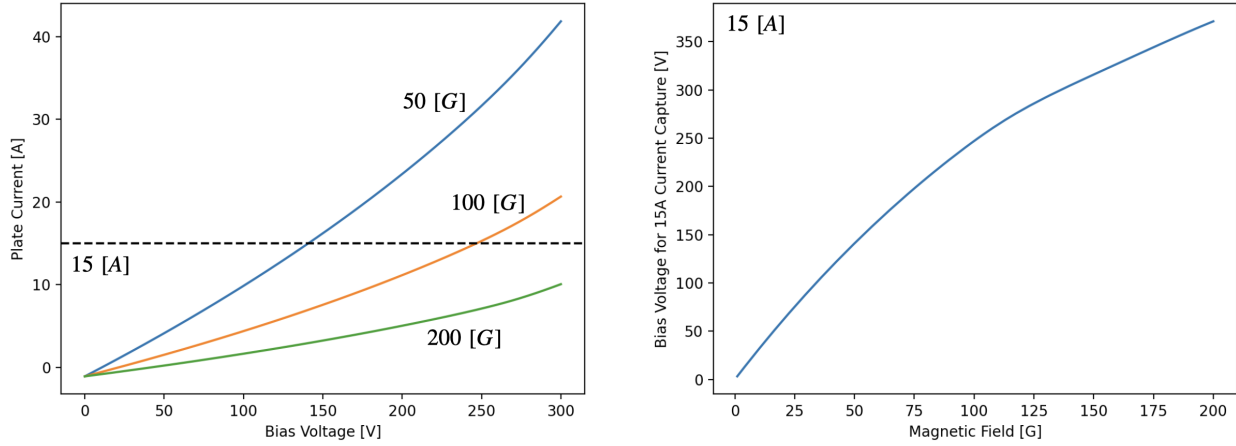


**Figure 3.** Theoretical curves for the total current to the plate as a function of applied bias voltage for three magnetic field strengths (left) and plot of the bias voltage needed to capture 15 A of current as a function of magnetic field strength (right). Functionally, the right graph plots the 15 A intersection voltage for each I-V curve in the left graph.

Furthermore, we can examine the effect of electron number density on the achievable bias voltage. As shown in Fig. 4, the bias voltage required to draw a steady amount of beam current on the plate decreases with electron number density at a steady magnetic field.

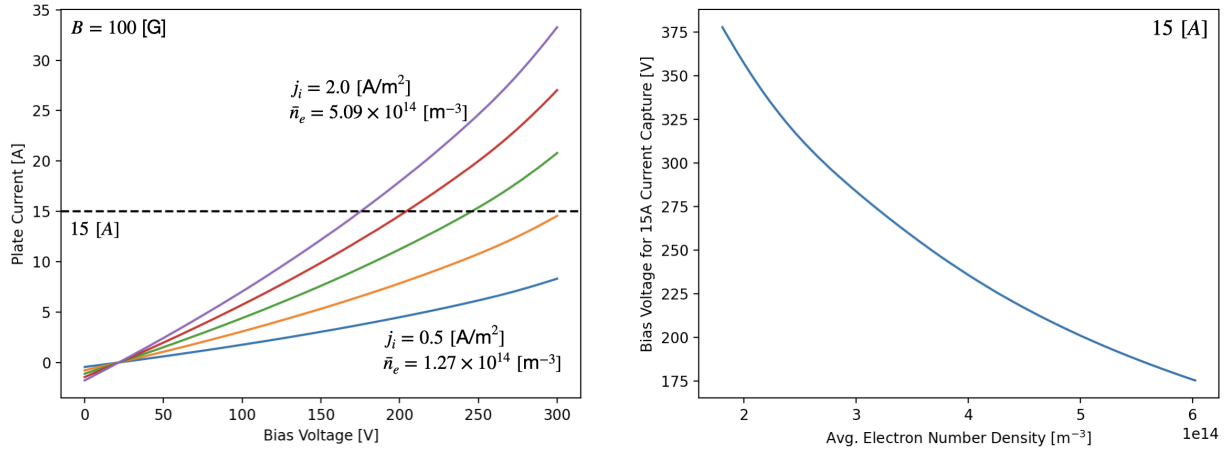


**Figure 4.** Theoretical curves for the total current to the plate as a function of applied bias voltage for varying current number densities (left) and plot of the bias voltage needed to capture 15 A of current as a function of average electron number density (right). Functionally, the right graph plots the 15 A intersection voltage for each I-V curve in the left graph. All plots use a fixed magnetic field strength of 100 G.

The level of plate bias sets the amount of ion retardation that can be achieved. Hence, when designing

a beam catcher in practice, these two aforementioned effects should be balanced. For instance, the current density at the beam catcher decreases with distance from the thruster, thereby reducing the achievable plate bias. To compensate, a magnetic field of sufficient strength should be applied to allow the beam catcher to capture the expected level of thruster beam current. Now that we have established the role of the magnetic field in isolating the beam catcher bias plate from the thruster plume and test environment, we turn to experimentally evaluating the efficacy of this approach.

### III. Experimental Setup

In this section, we describe our approach to experimentally evaluating a large-scale beam catcher in the plume of a Hall effect thruster. We first describe the design of the large-scale beam catcher prototype used in this study. We then describe the facility, thruster, and test configurations we employed.

#### A. Beam Catcher Design

In our previous work, we were unable to apply active biases to a beam catcher situated in the near-field of the H9 thruster due to strong coupling between the plate bias and the cathode-to-ground potential.<sup>17</sup> In this study we overcame this limitation by placing the beam catcher further away from the thruster (thereby reducing the current density at the plate). To subtend a larger fraction of the thruster plume at that greater distance, we correspondingly increased the size of the beam catcher. This ‘large scale’ design, illustrated in Fig. 5, is double the size of the configuration presented previously.<sup>17</sup> The large scale beam catcher consists of two graphite plates mounted side-by-side to achieve a total current capture area measuring  $1.33 \times 0.66$  m. These plates are mounted to a T-slot framing structure within five pill-shaped solenoids measuring approximately  $0.89 \times 0.49 \times 0.03$  m that function as Helmholtz coils, generating a uniform transverse magnetic field. The solenoids are comprised of 550 turns of 14-gauge polyamide insulated magnet wire and are spaced 0.29 m apart such that three span each square graphite plate.

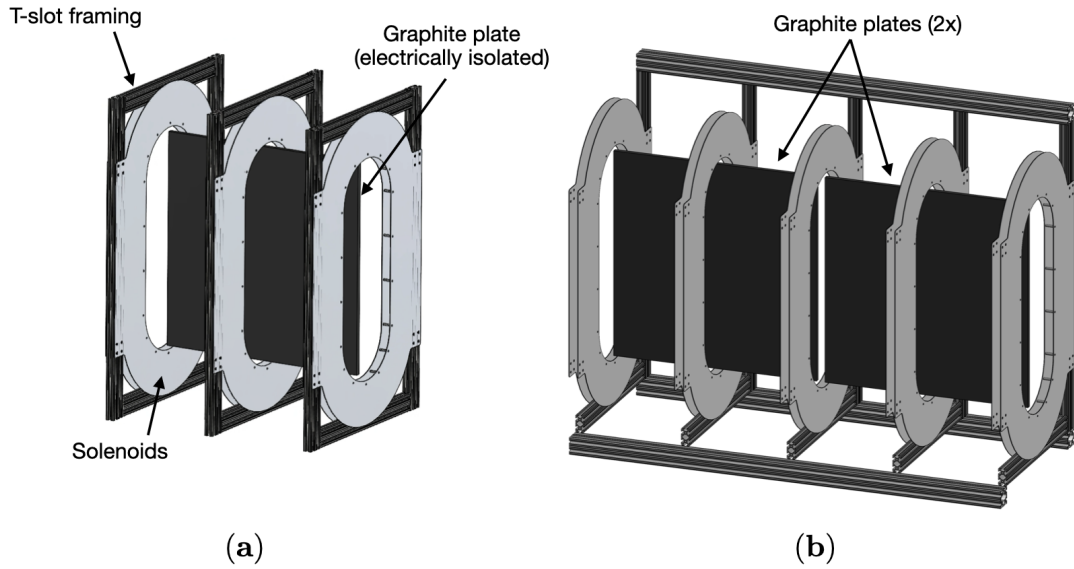


**Figure 5.** Computer models of the beam catcher in the three-coil, single-plate configuration (a) used in the previous study,<sup>17</sup> and in the 5-coil, double-plate configuration (b) used in this study.

The parallel solenoids produce a generally uniform magnetic field transverse to the plate. The transverse field strength is nominally 100 G for 5 A of current and 200 G for 10 A. The portions of the solenoid coils in front of the plate present a sputtering target and so were covered in graphite felt. We simulated the magnetic field strength and topology in COMSOL Multiphysics for solenoids modeled as homogenized multi-turn conductors with 3000 Amp-turns. Fig. 6 shows the results of this simulation for the five-coil configuration. The parallel coil configuration produces a strong magnetic field within and a weak field

outside of the solenoids. To capture the largest fraction of the ion beam, we aligned the center of the bias plates with the center of the thruster. We used aluminum T-slot framing to both support the pill shaped solenoids and assist with alignment. We covered all exposed parts of the frame and support structures in graphite felt to reduce sputter yield from the aluminum bars.

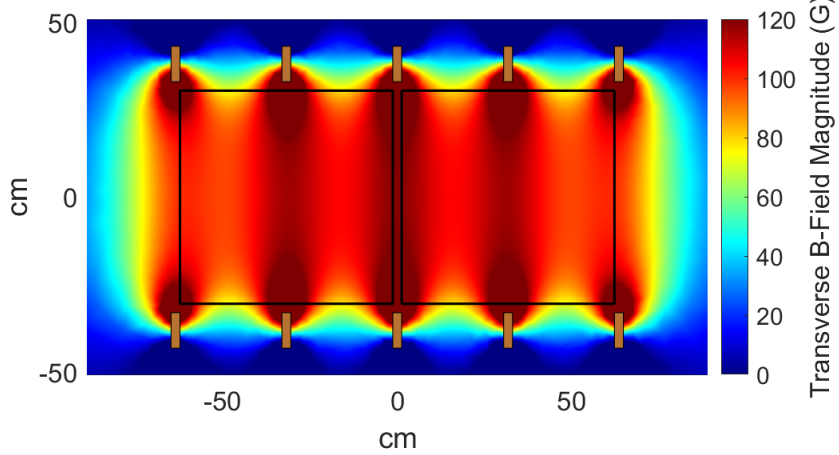


**Figure 6.** Front view of the beam catcher COMSOL simulation of transverse magnetic field strength at 5A of applied solenoid current.

## B. Facility and thruster

We used the H9 magnetically-shielded laboratory Hall thruster operating on krypton as the ion source for these tests. The H9 thruster is a 9 kW class Hall thruster developed jointly by the Jet Propulsion Laboratory, the University of Michigan, and the Air Force Research Laboratory as a common test article for Hall effect thruster research. As described by Hofer et al.,<sup>21</sup> the discharge chamber is comprised of boron nitride, the anode of stainless steel, and magnetic pole covers of graphite. It also employs a center-mounted lanthanum hexaboride ( $\text{LaB}_6$ ) hollow cathode. We operated the thruster on krypton gas at a discharge voltage of 300 V and current of 15 A for all tests reported in this study. We conducted the experiments inside the Alec D. Gallimore Large Vacuum Test Facility (LVTF) chamber at the University of Michigan. LVTF measures 6 m in diameter by 9 m in length and employs nineteen cryopumps to achieve a measured pumping speed of 600,000 L/s for krypton.<sup>18</sup>

## C. Test configuration

In our previous work, we tested the small scale beam catcher in the near field of the H9 thruster.<sup>17</sup> That placement was motivated by the desire to subtend a large fraction of the thruster plume with a small beam catcher surface area. We ultimately observed a 20% reduction in backscatter for a 300 V thruster discharge, but were unable to bias the plate above floating because doing so would cause a large rise in cathode floating voltage relative to ground. Therefore, although the beam catcher was subtending most of the beam, its ability to retard the ion energy was curtailed by its close proximity. Indeed, per Eq. 13, we see that electron current is increased if the local density is higher (a function of the enhanced collisionality induced by a higher particle density). This suggests that moving the beam catcher farther from the thruster may improve the attainable retarding potential and by extension reduce sputter further—even if less of the overall beam is subtended. This conclusion is supported by previous work by Thompson et al. performed on a gridded ion source that showed that the floating voltage reached by the beam catcher plate increases with distance from the thruster.<sup>16</sup>

An additional challenge previously observed by Thompson et al. was the production of negative backscatter rates at high bias voltages.<sup>16</sup> We previously theorized that this is caused by erosion from ions launched back at the thruster by the beam catcher.<sup>17</sup> We hypothesize that these ions are born from slow-moving neutrals near the bias plate via charge exchange (CEX). Born with low velocities, these ions are then accelerated

towards the thruster by the bias plate and the beam catcher becomes a reverse Hall thruster. To mitigate this problem, we proposed moving the beam catcher further from the thruster to reduce the plasma (and therefore neutral) density at the plate and preclude the production of CEX ions.<sup>17</sup>

To both enhance ion retardation and reduce the rate of CEX ion production, in this study we chose to place the beam catcher 2.5 m downstream of the thruster, greatly exceeding the distances used in either previous study.<sup>16,17</sup> Using ion beam distribution measurements taken with the beam catcher off and the geometric configuration of this test setup, we estimate that the bias plates subtended 47% of the beam current.

We also angled the beam catcher by 10° with the goal of deflecting CEX-born ions towards cryogenic shrouds located to the side of the thruster.<sup>18</sup> This configuration is illustrated in Fig. 7. Behind the beam catcher, we left the permanently installed graphite panels that serve as LVTF's standard beam dump. These panels approximately span the entire open area and are angled to deflect neutrals to the sides of the chamber.<sup>18</sup>

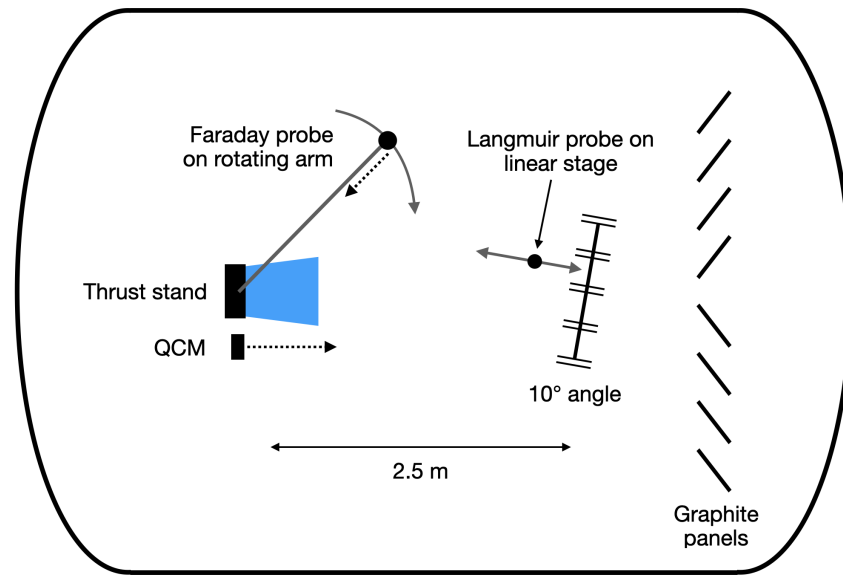


**Figure 7.** Notional top view diagram of the experimental setup we used to study the beam catcher. Dotted arrows indicate the direction of open apertures for relevant diagnostics.

In this configuration, we measured the backspatter rate at the thruster plane using a quartz crystal microbalance (QCM) and employed a Langmuir probe, Faraday probe, thrust stand, and differential voltage probe to characterize the effect of the beam catcher on the thruster. The locations of these probes are illustrated notionally in Fig. 7. The Faraday probe was mounted facing the thruster on a rotating arm in front of the beam catcher. The Langmuir probe was mounted on a linear stage so that it could take measurements in both the far field plume and inside the magnetic field region of the beam catcher. Specifics about how we placed, operated, and processed the data from each diagnostic are given in Sec. IV. In addition to these five diagnostic instruments, we placed an ion gauge near the thruster to measure the local pressure and recorded the beam catcher plate current needed to maintain a constant plate potential bias. The parameters we varied during the study were solenoid current and beam dump bias potential.

#### IV. Diagnostics

In this study we aimed to characterize backspatter rate and to validate our assumption that the beam catcher does not significantly impact thruster operation. To characterize backspatter, we used a QCM to directly measure the net deposition rate of backspattered material at the thruster. To evaluate the impact on thruster operation, we used a Langmuir probe, swept Faraday probe, current probe, and thrust stand. In this section, we provide descriptions of how we used the aforementioned diagnostic tools and analyzed their data.

## A. Quartz Crystal Microbalance

A QCM is a mass measurement device commonly used to measure the real time deposition of a thin film. It works by measuring the resonant frequency of a quartz crystal, which varies with mass deposited (or removed from) the crystal surface. We used a QCM to measure net backscatter deposition rates at the thruster plane. In all test configurations, we mounted the QCM adjacent to the thruster at center line height, facing downstream to capture material sputtered from the beam catcher.

For accurate mass readings, temperature stabilization was critical due to temperature effects on resonant frequency. We employed passive liquid cooling and radiation shielding to maintain the QCM within a 1-3 degree temperature window, a range we previously established as having negligible impact on deposition rate measurements.<sup>17</sup> In situ, we recorded the QCM frequency at a 1 Hz sample rate over a five minute measurement window and discarded the first 100 seconds of data as a settling period. We then converted frequency data to film thickness via the Z-match equation developed by Lu and Lewis.<sup>22</sup> To compute the backscatter rate, we fit a line to the film thickness data.

To quantify uncertainty in the linear fits, we performed statistical bootstrapping on the dataset. For the 200 data points in the measurement set, we sampled 200 points with repetition, performed a linear fit to the sample, and repeated 10,000 times. We took the mean of the fits to be the most likely deposition rate and the standard deviation to be the uncertainty.

## B. Langmuir Probe

In this experiment, we employed a planar Langmuir probe mounted parallel to the direction of the ion beam on a motion stage to measure the plasma potential in front of (and within) the magnetic field region of the beam catcher to thereby assess the effect of the beam catcher plate bias on the main thruster beam.

We found the plasma potential from this diagnostic by employing the so-called knee technique.<sup>23</sup> We employed seven knee finding algorithms on the I-V trace to form a ‘distribution’ of inflection points: first derivative maximum; second derivative zero; second derivative first peak; bisector and kneedle<sup>24</sup> on current natural logarithm; bisector and kneedle on first derivative. We took the mean of these points to be the plasma potential and the standard deviation to be the error band. We then subtracted the cathode to ground voltage from the measurement mean so that the plasma potential is measured with respect to (w.r.t.) the cathode potential. This correction is necessary because the Langmuir probe measurement is made w.r.t facility ground while the cathode-to-ground voltage is variable with plate bias.

In this study, we mounted the Langmuir probe at thruster center line height on a linear stage perpendicular to the beam catcher bias plate. The stage allowed the instrument to take measurements in both the far field beam plasma (outside of the magnetic field region) and the plasma within the magnetic field region. We took measurements at three locations, each separated by 30 cm. The first point was located inside the magnetic coils, 2.9 cm from the plate surface (this was the closest to the plate we could feasibly move the probe). The second point was located 30 cm back, right outside the electromagnetic coil. The third point was another 30 cm back so as to be in the thruster far-field plume. Fig. 8 illustrates the relative positions of these three measurement points.

## C. Faraday Probe

To characterize the spatial distribution of the plume, we mounted a nude Faraday probe to a rotating arm facing the thruster, as depicted in Fig. 7. We swept the probe 180° across the front of the thruster (from one side of the thruster to the other). We then examined the current density distribution as a function of angle. An example of a typical Faraday probe current density distribution trace for a Hall thruster is shown in Fig. 9. The twin peaks in the trace correspond to the thruster channel openings.

## D. Thrust Stand

To measure thrust, we used an inverted pendulum thrust stand operating in null displacement mode.<sup>25,26</sup> In this measurement scheme, the thruster is mounted to a plate atop a flexure (this comprises the inverted pendulum) which is held upright by force from a load spring and a “null coil” solenoid.<sup>25</sup> This entire assembly is mounted to a pivot arm which enables active compensation for the weight of the thruster. During thruster operation, the device actively monitors the inclination of the inverted pendulum and varies the current to the null coil to provide a restoring force against the thrust produced by the Hall thruster. Prior to testing,

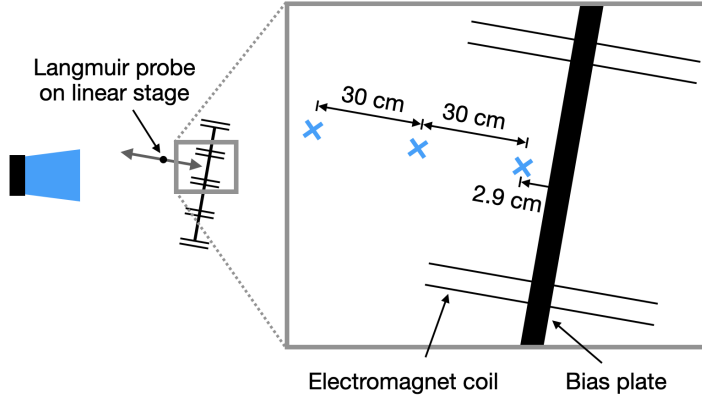


**Figure 8.** Notional diagram showing the location of Langmuir probe measurements as blue X's.

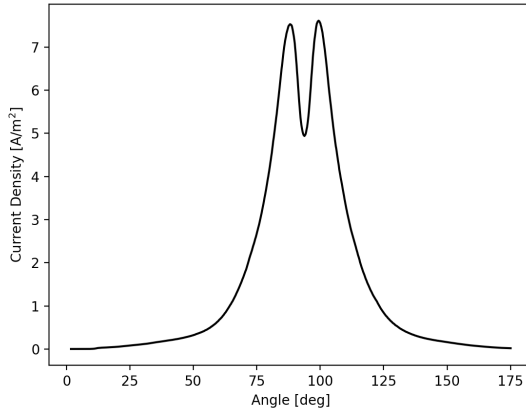


**Figure 9.** Faraday probe trace of the H9 Hall thruster operating on krypton at 300V, 15A without the beam catcher powered on. The thruster center line is located at 90°.

we employed a known set of calibration masses corresponding to weights of 45 mN to 1 N to correlate the change in null coil current to applied force. This calibration yielded a linear fit of the form

$$\Delta I_N = s(T/g) + b, \quad (17)$$

where  $\Delta I_N$  is the change in null coil current,  $s$  is the calibration slope,  $b$  is the calibration line intercept,  $g$  is the gravitational constant, and  $T$  is the thrust (calibration weight) imparted. We determined  $b$  by fitting a line to the calibration data. To determine thrust, we invert the above equation to yield thrust as a function of the null coil current,  $T = (\Delta I_n - b)g/s$ .

The major sources of error for this thrust stand are the calibration slope and intercept ( $\delta s, \delta b$ ), the change in inclination angle ( $\Delta\gamma$ ), and the noise in the null coil current signal. We estimate the uncertainty in the slope and intercept as the 95% confidence intervals of the fit. We calculate the uncertainty in thrust due to a change in inclination angle as  $mg \sin \Delta\gamma$ , where  $m$  is the mass of the thruster. We approximated the uncertainty in the null coil current  $I_N$  by taking the standard error over 40 points before and after shutdown. We combine these uncertainty modes in quadrature to find that the average thrust uncertainty for each experimental condition. In general, this uncertainty is approximately 6% of the measured thrust.

## E. Differential Probes

We recorded high frequency oscillations in the anode current with a pair of Tektronix P5200A high voltage differential probes connected to a Keysight DSOX3024A oscilloscope. We recorded probe measurements for a duration of 0.003 s at a sample rate of  $3.125 \times 10^7$  Hz. To compare thruster oscillations we obtained a power spectrum at each beam catcher operating condition. To obtain smoother measurements, we split the raw measurement into ten equally sized samples in the time domain, calculated the magnitude of the fast Fourier transform of the recorded oscillation for each, and obtained the median of the results frequency-wise across all ten samples. Given the sample length and Nyquist frequency, the resolvable frequency spectrum was  $3 \times 10^3$  to  $3.125 \times 10^7$ . An example power spectrum is shown in Fig. 10.

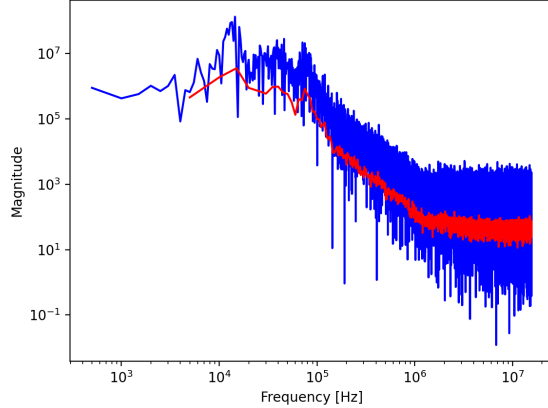


**Figure 10.** Example full time domain (blue) and time domain window-sampled (red) power spectra obtained from the Fourier transform of recorded anode current oscillations.

## V. Results

In this passage, we first report the achievable range of plate biases for this configuration and then the level of backscatter reduction achieved and how the cathode-to-ground voltage varies with beam catcher operating condition. We then report the following metrics relevant to thruster performance: plasma potential, thrust level, plume divergence, and oscillations in anode current and cathode-to-ground voltage.

### A. Achievable Plate Biases

To characterize the accessible range of retarding potentials in the far-field configuration, we swept the applied bias voltage and magnetic field of the beam catcher. For the active bias sweep, we recorded the plate power supply current necessary to maintain said bias. For the magnetic field sweep, we recorded the attained floating voltage. We also recorded the cathode-to-ground voltage at each bias condition.

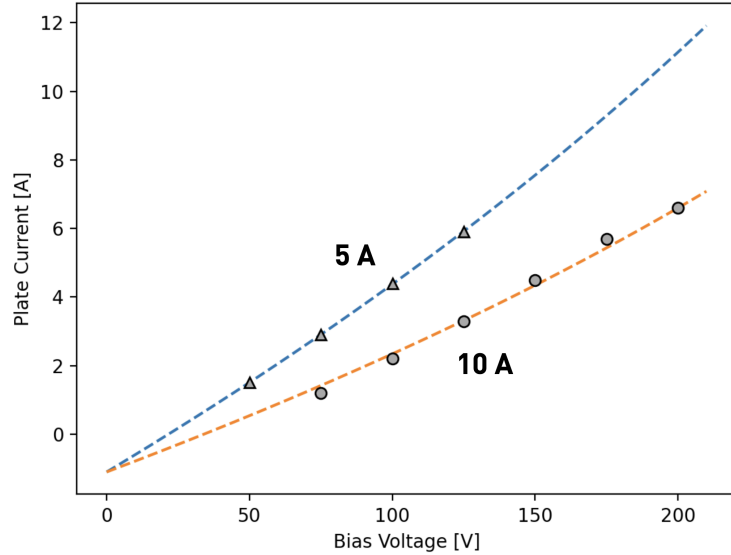
#### 1. Active Bias

Figure 11 shows the plate current necessary to maintain an active bias at a constant magnetic field strength. The triangles correspond to data for a 5 A magnetic field strength and the blue curve represents Eq. 16 fitted for a 100 G magnetic field. The circles correspond to data for a 10 A magnetic field strength and the orange curve represents Eq. 16 fitted for a 159 G magnetic field. These trends are physically consistent with the theory which predicts that, for a fixed bias voltage, a larger magnetic field results in lower electron current to the plate. Practically, this result demonstrates that stronger magnetic fields enable higher retarding biases to be achieved for a lower current draw at the plate.

We obtained the curves in Fig. 11 were obtained by regressing Eq. 16 to data collected at a magnetic field strength of 100 G. In this regression, we treated the electron collision Bohm scaling coefficient (i.e. the  $\alpha$  in  $\nu = \alpha\omega_e$ ), potential drop region length  $L$ , and far-field plume current density  $j_i$  as free parameters. This yielded fit parameters  $\alpha = 0.12$ ,  $L = 0.01$  m, and  $j_i = 1.24$  A/m<sup>2</sup>.

There are two significant physical implications of these fit parameters. First, the fit length scale  $L$  is a single centimeter, an order of magnitude below the length scale of the magnetic field region. This implies that the potential drop (the region where ion deceleration actually occurs) is concentrated near the edge of the bias plate. This is commensurate with plume potential measurements shown in Sec. V.C.1, where the plasma potential remains largely invariant up to 3 cm in front of the plate.

Second, the Bohm scaling coefficient yields a collision frequency of  $2.45 \times 10^8$  Hz, five orders of magnitude larger than expected by classical electron-ion collisions (which predict  $\sim 10^3$  Hz in our system). This indicates that additional processes are occurring which enhance electron mobility to the plate. We discuss both the collision frequency and deceleration region length in greater detail in Sec. VI.



**Figure 11.** Sweeps of active bias voltage and requisite plate power supply current at 5 A (triangles) and 10 A (circles) of applied magnet current. These currents correspond to magnetic fields strengths of 100 G and 200 G, respectively. The blue and orange curves represent Eq. 16 evaluated for a 100 G and 159 G magnetic field, respectively, using the aforementioned fit parameters.

## 2. Cathode-to-Ground Potential

Regardless of the magnetic field strength, the beam catcher draws electron current from the beam proportionally with the bias voltage. Because the thruster/cathode system is allowed to float in situ, we monitored the cathode-to-facility-ground (C2G) potential. Figure 12 shows a plot of C2G voltage at two constant applied magnetic field strengths. The more gradual rise in the C2G voltage for 10 A of magnet current is commensurate with theory – Eq. 16 shows that for a fixed amount of electron current (which induces a C2G voltage rise), a larger magnetic field strength enables a larger bias voltage to be held off.

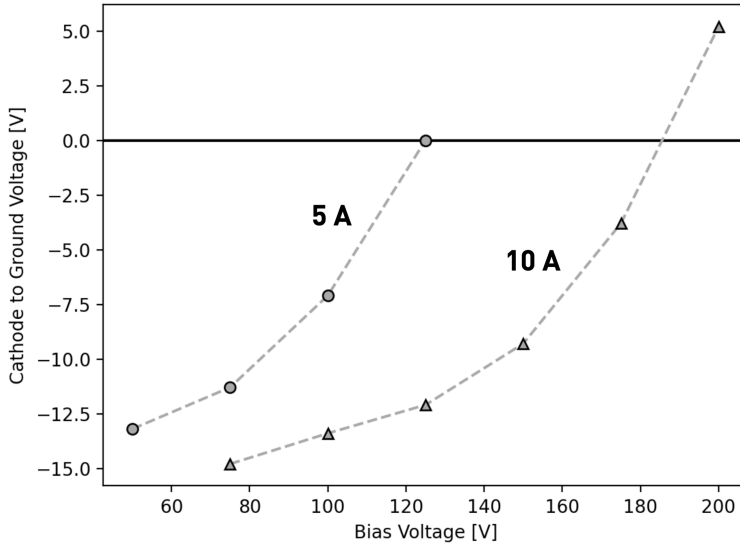


Figure 12. Cathode-to-ground potential as a function of applied bias voltage at 5 A and 10 A of magnetic current.

### B. Backsputter Reduction

During testing, we took backsputter rate measurements at five operating conditions. In each case the plate was actively biased with respect to facility ground. We allowed the thruster/cathode system to float in situ and recorded the cathode-to-ground (C2G) voltage. The effective ion retarding potential is therefore the difference between the bias voltage and the C2G voltage. Figure 13 plots the net backsputter rates as a function of ion retarding potential. Preliminarily, this indicates that the beam catcher is effective at potentially eliminating erosion. We note, however, that the erosion rates become negative at sufficiently high bias potentials, a non-physical result. A possible explanation for this is that energetic charge exchange ions are being launched back at the QCM by the beam catcher. We expand on this point in Sec. VI.

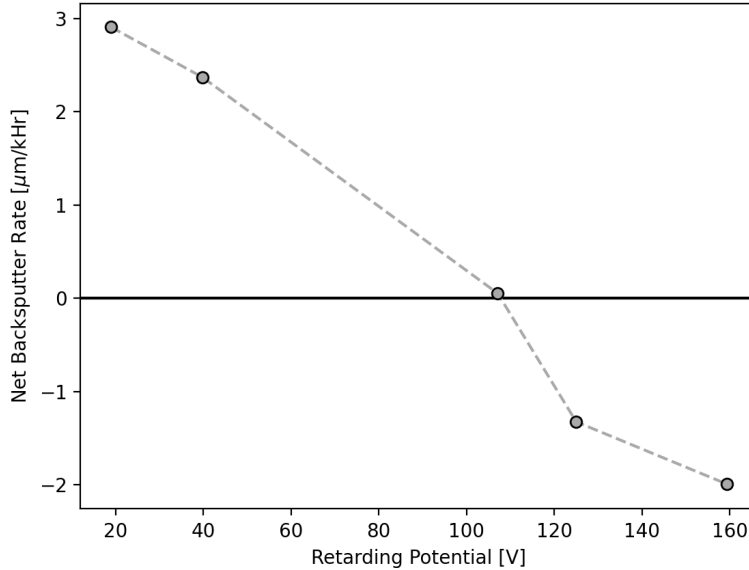


Figure 13. Net backsputter rate as a function of ion retarding potential.

In summary, we have found that from an electrical standpoint the beam catcher responds consistently with our simplified theory. It is able to support large plate biases with only minimal impacts on the adjacent plasma. Correspondingly, it has a direct result on backscatter. While these results provide initial validation of this proof of concept, there remains an open question as to whether the beam dump impacts thruster operation. We turn to this question in our next section

### C. Impact on Thruster Operation

To evaluate the impact of the beam catcher on thruster operation, we recorded four key metrics: far field plasma potential, thrust level, plume divergence, and anode current oscillations.

#### 1. Far-Field Plume Potential

The potential of the far-field thruster plume was of key interest to us because an invariant plume potential in the presence of a plate bias confirms the beam catcher concept of operation (namely that the magnetic field can decouple the bias plate and plume potentials). As shown in Fig. 8, we measured the plasma potential as a function of bias voltage at three locations: 2.9 cm from the plate surface (as near the plate as was possible to measure); 30 cm further back, at the edge of the solenoid; and another 30 cm further back, in the far-field plume. To ensure that the changes in plume potential between bias cases may be compared directly to one another in spite of the variable cathode-to-ground potential, we report the thruster plume with respect to cathode potential (rather than facility ground) as described in Sec. IV.B. The results of the plasma potential measurements are shown in Fig. 14.

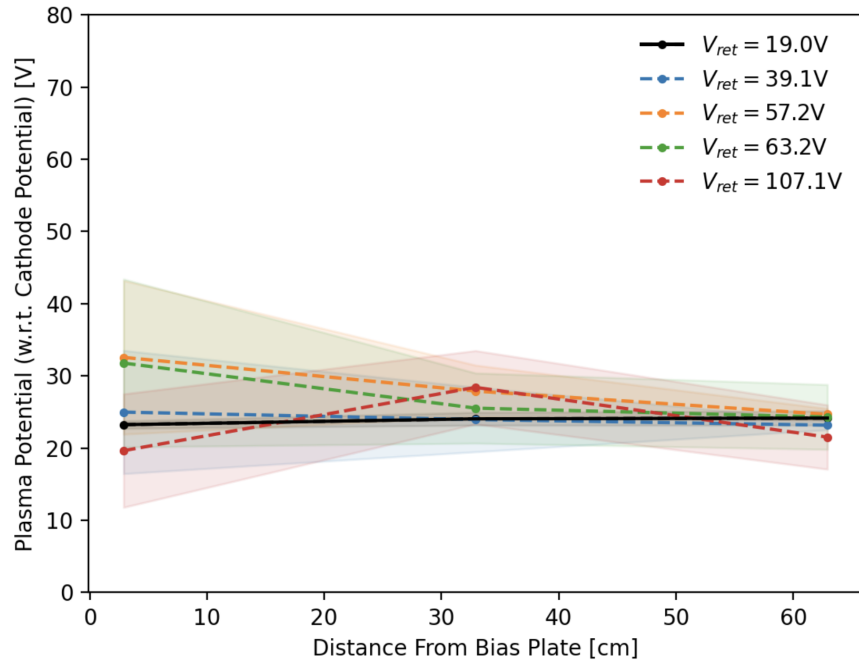


**Figure 14.** Plasma potential as a function of distance from the bias plate at five retarding biases,  $V_{ret}$ . The black line ( $V_{ret} = 19\text{V}$ ) represents the baseline case with the beam catcher powered off.

There are two key takeaways of note. First, the far-field plume potential (63 cm from the plate) remains nearly invariant at any applied plate bias. This confirms that the magnetic field is successfully decoupling the plate and plume potentials. Second, the plasma potential generally appears to increase with both proximity to the plate and applied bias, as evidenced by the divergence in means as distance increases. That being said, we further note that the error bars of all measurements overlap partially at all test conditions, indicating that within error the plasma potential could be invariant to within 2.9 cm of the plate surface. This would suggest physically that increases in plasma potential resulting from the applied potential are localized to the region immediately adjacent to the plate surface. We return to a discussion of this result in VI.

## 2. Plume Current Distribution

Figure 15 shows a superposition of raw Faraday probe traces taken at a variety of plate biases. By inspection, the wings of the traces become more pronounced with increasing plate bias and the data show a corresponding attenuation in peak current with increasing bias. This result thus does in fact show there is an influence of the beam catcher on at least downstream aspects of the thruster operation. Notably, this response is similar to trends that have been previously reported for current density profiles in response to increase facility pressure. This may point to the possibility that the beam catcher is locally increasing the neutral density in the facility with increasing applied bias. We return to this point in Sec. VI.

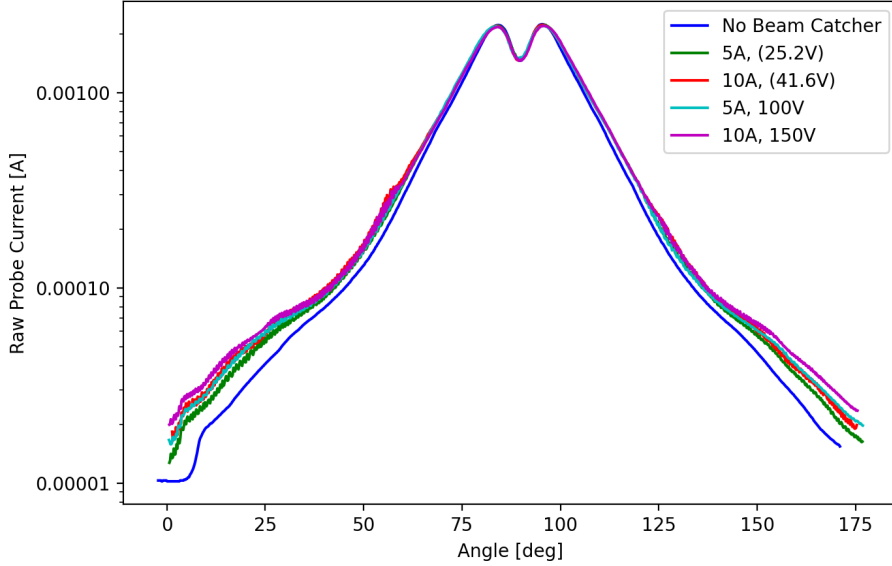


**Figure 15.** Raw Faraday probe traces at a sweep of plate bias potentials. The legend denotes solenoid current and plate bias, with floating voltages marked by parentheses.

## 3. Thrust

Figure 16 shows measurements of thrust with increasing plate bias. In all cases, the variance in mean measured thrust does not exceed 10 mN and the error bars overlap with the baseline condition. This allows us to conclude that thrust levels are unchanged by the presence of this beam dump, even in the presence of large retarding potentials.

## 4. Anode Current Oscillations

Figure 17 shows the oscillation power spectra for anode current with the beam catcher powered off and at a 100 V bias. The peak in anode current fluctuations near 10 kHz is consistent with a canonical breathing mode oscillation.<sup>27</sup> By inspection, the power spectra share peaks in at near identical frequencies, demonstrating that the beam catcher does not affect thruster oscillations.

In summary, we have found that three key aspects of thruster operation are not impacted by the beam catcher bias: far-field plume potential, thrust, and anode current oscillations. We also found that the plume distribution responds by effectively widening with higher applied biases. In the next section, we expand on these results and their implications for the efficacy of this approach for backscatter mitigation.

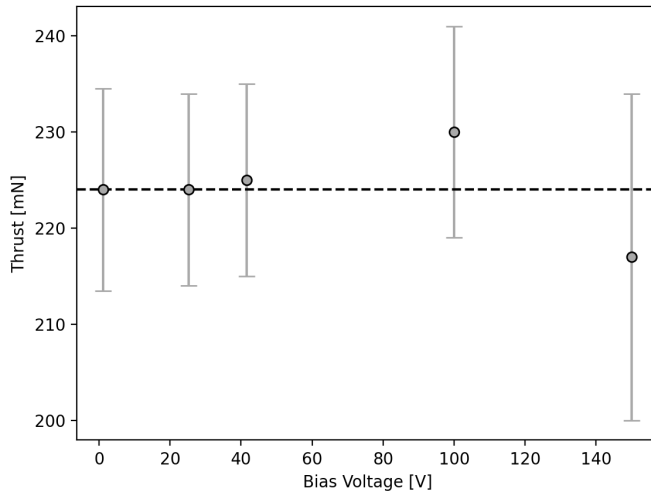


Figure 16. Thrust measurements at a sweep of plate bias potentials. The dotted line marks the baseline condition (beam catcher powered off).

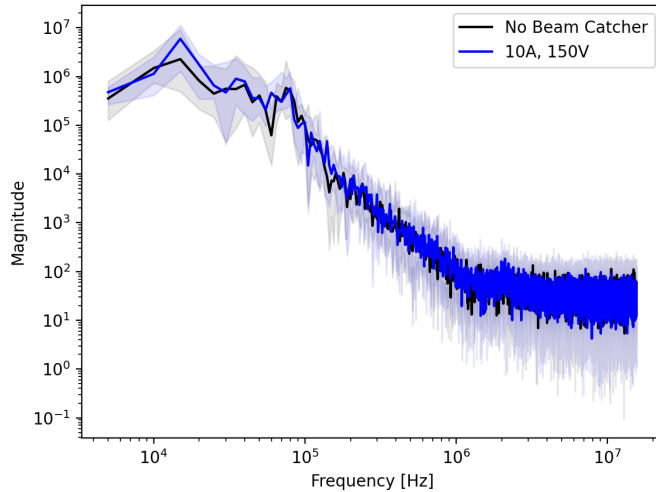


Figure 17. Oscillation power spectrum of anode current with the beam catcher powered off (black) and at 5 A solenoid current, 100 V bias (blue). The colored bands denote the 80th percentile of the time-domain samples.

## VI. Discussion

The aforementioned results confirm that the thruster's far-field plume potential, thrust levels, and anode current oscillations are unaffected by the beam catcher, even at high biases. However, they also introduce results requiring further explanation. In this section we discuss the findings of increased plume divergence, low plasma potentials near the bias plate, and negative backscatter rates. We also discuss the limitations and implications of the 0D model presented in Sec. II.

### A. Far-Field Divergence

In Fig. 15, we observe an increase in beam divergence with increasing plate bias. Such an increase in divergence typically follows an increase in background neutral density. Higher background neutral densities

drive higher rates of ion-neutral collisions, which in turn have the effect of scattering beam ions. This scattering manifests in a Faraday probe trace as an attenuation of peak beam current and a broadening of the trace's wings as beam ions are scattered into the edges of the trace. These are the same symptoms visible in Fig. 15.

We hypothesize that an increase in background neutral density comes as an effect of placing the beam catcher inside the main thruster beam. Ions that strike the plate are neutralized and reflected back towards the incoming ion beam, increasing the local neutral density in front of the plate. This effect is visible to the eye as a glow cloud during operation of the beam catcher at high bias voltages, as shown in Fig. 18. The brightness of the glow shown in Fig. 18 qualitatively increased with plate bias. We believe that the glow is caused by excitation of a locally high density cloud of neutrals directly in front of the beam catcher interacting with both incoming high-energy ions from the thruster and outgoing CEX-generated ions being launched by the beam catcher.



**Figure 18.** Photograph of the beam catcher operating at 5 A solenoid current 100 V bias (left) in the presence of an H9 thruster beam (right).

Neutral density may be correlated with plate bias if a fraction of incoming ions experience specular collisions with the bias plate (this is typically represented by the specular accommodation coefficient). In the absence of a retarding potential, specular high-energy ions would reflect as neutrals off the plate at the same speed at which they entered. In the presence of a retarding potential, however, the incoming ions would be slowed prior to experiencing a neutralizing collision, hence would reflect back at a lower speed. For particle continuity to be maintained, this reduction in the speed of reflected neutrals dictates that the number density must increase. This theory is corroborated by ion gauge measurements of background chamber pressure at the thruster plane (shown in Table 1) which increased with applied bias potential.

Plate Bias [V]	Pressure [Torr]
(1.15)	$1.08 \times 10^{-5}$
(25.2)	$1.09 \times 10^{-5}$
41.6	$1.10 \times 10^{-5}$
100	$1.11 \times 10^{-5}$
150	$1.14 \times 10^{-5}$

**Table 1.** Background pressures measured at the thruster plane. Parenthetical biases represent floating voltages.

Mitigations for this effect rely on reducing the neutral density. One potential method of achieving this reduction is to replace the bias plate with a grid that has a hole spacing that is smaller than the Debye length of the plasma but larger than a few neutral diameters (this has the effect of being opaque to ions but transparent to neutrals). By allowing neutral flux to pass through the beam catcher, the number density in front of the beam catcher may be reduced. Another potential mitigation is to angle the beam catcher to deflect neutrals away from the thruster plume. Although the local neutral density would remain high in

the directions of deflection, the neutral density in the path of the beam (which contributes to scattering the beam) could effectively remain low.

## B. Near-Plate Plasma Potential

Within the magnetic field region of the beam catcher (near the bias plate), we expect to see the plasma potential rise with bias voltage. This would correspond to the magnetic field acting as an impedance region. However, in Fig. 14 we do not observe a clear trend in near-plate plasma potential with increasing plate bias. This observation is complicated further by the uncertainty bands which are large enough to include the near-plate baseline condition (beam catcher off) in all cases. This implies that it is possible for the plate-to-plasma potential drop to be tightly concentrated at the plate surface. This is corroborated by the results of regressing Eq. 16 to the data shown in Fig. 4, which yields a length scale for the potential drop region on the order of 1 cm. We were only able to maneuver our Langmuir probe to a minimum distance of 2.9 cm from the plate, hence it is possible that we were unable to measure the drop region directly.

This concentration of the drop region directly in front of the plate may be caused by the magnetic field being non-uniform in the plate-normal direction, as shown in Fig. 19. We note that our previous assumption of a linear potential drop requires a uniform plate-normal magnetic field in the drop region. Although the magnetic field simulation of Fig. 6 shows a relatively uniform field across the plane of the plates, Fig. 19 shows that in the plate-normal direction, the magnetic field strength varies non-linearly with distance from the plate.

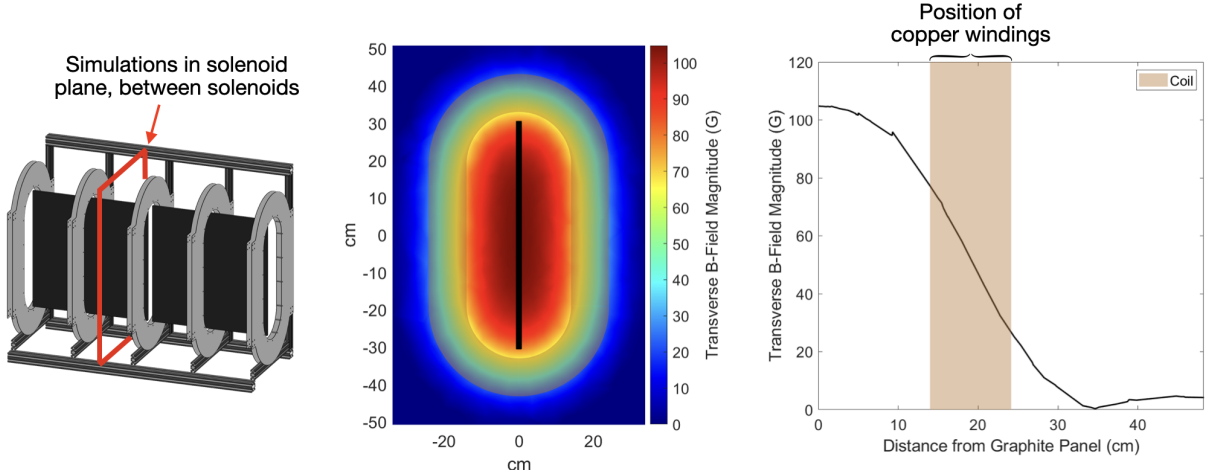


**Figure 19. COMSOL simulations of the solenoid-plane magnetic field strength between solenoids.**

Although mitigations for this potential drop might be achieved through careful shaping of the beam catcher magnetic field, it is unclear whether this would hold any practical benefit. Regardless of where the potential drop occurs, the existence of any drop region between the bias plate and the far-field plume serves to decouple the plate bias from the thruster plume and would enable the beam catcher to operate in its intended manner. Indeed, the results from this study show that irrespective of where the potential drop actually occurs in this device, backscatter rates can be reduced while minimally affecting thruster operation.

## C. Limitations of the 0D Model

When fitting the 0D current model given by Eq. 16 to experimental data, we inferred two free parameters: potential drop region length and electron collision frequency. The physicality of the former was discussed in the previous section. The latter, however, is highly non-physical for classical collisions. The collision frequency we inferred was  $\nu = 2.45 \times 10^8$  Hz. By comparison, the electron-ion collision frequency for realistic plasma parameters in this experiment was  $\nu_{ei} = 2.65 \times 10^3$  Hz. In an effort to boost the total collision frequency, we calculated the electron-neutral collision frequency using a model for krypton-electron by Baille et al.<sup>28</sup> To maximize the neutral density, we assumed fully diffuse collisions between ions and a 200° C bias

plate. This estimate yielded a collision frequency of  $\nu_{en} = 1.18 \times 10^5$  Hz, two orders of magnitude higher than electron-ion collisions, but still significantly below the inferred  $10^8$  Hz.

The significance of the collisional frequency parameter is most easily seen in the electron current density equation, Eq. 5, which is a form of Ohm's law. Here, it is apparent that  $\nu$  drives the conductance of the modeled system. Hence, high values of  $\nu$  indicate higher levels of electron mobility to the plate than can be explained by classical ion or neutral collisions alone. A potential explanation for this is that the beam catcher is not a closed-drift system; electron current may be collected on the edges of the plate where the magnetic field lines of the solenoid terminate.

Let us consider electrons to travel at their thermal speed along magnetic field lines to eventually terminate at the plate edge. We may capture the effect of this electron thermal drift by scaling the collision frequency with the ratio of the electron thermal speed to a characteristic length,  $\nu_\tau = v_{th}/l$ . Taking  $l$  to be the length of the beam catcher, this ratio describes the time over which an electron may traverse the beam catcher length. For 2 eV electrons,  $\nu_\tau$  is of order  $10^5$  for the beam catcher length scale of 1 m, again too low to describe electron transport in this system. It may be possible to boost  $\nu_\tau$  further by assuming an electric field component parallel to the magnetic field lines (increasing the velocity of the electrons), but it is not immediately apparent how we would quantify that effect in a model.

Ultimately, we were able to fit Eq. 16 by assuming Bohm-like scaling of the collision frequency,  $\nu = \alpha w_e$ . Here, we considered  $\alpha$  to be a free parameter which we inferred via regression to be  $\alpha = 0.12$ . Although this scaling allows the 0D model to fit the data, the physical basis for it is not readily apparent. This highlights the fact that our model inherently attempts to fit a 0D model to a 3D system and is therefore limited in its ability to describe the system.

#### D. Backstreaming Ions & Negative Backspatter

In this study we observed significant negative backspatter rates at applied biases in excess of 100 V. We believe that these negative rates correspond to material being eroded off the QCM surface by ions launched by the beam catcher. The mechanism by which ion backstreaming occurs is illustrated in Fig. 20. High velocity ions streaming from the thruster (1) enter a region of high neutral density directly in front of the plate. Inside this region, high speed ions undergo charge exchange with low speed neutrals (2) to produce low speed ions. These ions, born near the plate bias, are accelerated away from the beam catcher (3) as a result of the potential difference between the bias plate and far-field plume (4). The consequence of this process is a stream of ions being launched back at the thruster at a fraction of the bias potential.

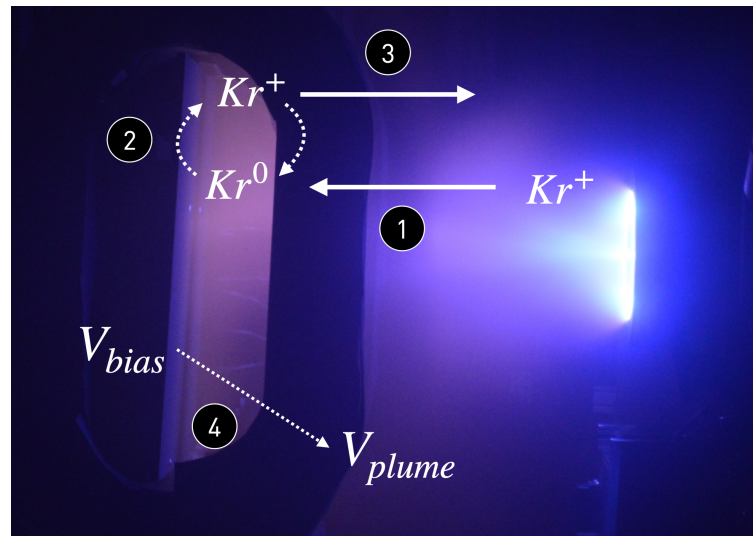


**Figure 20. Illustration of how charge exchange may drive ion backstreaming and erosion processes**

We corroborated this theory by placing a retarding potential analyzer (RPA) adjacent to the QCM during follow-on characterization of the small-scale beam dump initially tested by Hurley et al.<sup>17</sup> In these measurements, we found that for a near-field beam dump biased to 100 V and 150 V, the most probable

voltages for back-launched ions were 69.8 V and 96.4 V respectively. Unfortunately, RPA measurements could not successfully be made in this far-field study due to instrument malfunction.

To reduce the rate of CEX ion production, the neutral density in front of the plate should be reduced. This might be achieved using any of the manners suggested in Sec. VI.A, which discusses plume divergence mitigation. However, by nature of these back-launched ions being electrically charged, the additional strategy of deliberately directing ion direction by means of shaping the beam catcher's electric field may be employed. For an electric field that emanates normal to the bias plate, angling the beam dump to accelerate ions to either side of the thruster (or ideally towards a pump) may sufficiently mitigate ion backstreaming. We attempted to do this in this study by angling the beam catcher 10° off normal of the incoming ion beam, but presume that this angle was insufficient given the large lateral width of the beam catcher. In a future iteration, a wedge-shaped beam catcher employing two bias plates angled in opposite directions might be a practical implementation.

We note that the presence of negative backscatter rates highlight two limitations of this study. First, that the measurements taken in this study were insufficient to characterize the population of backstreaming ions. In this far-field study, neither the energy distribution nor current density of back-launched ions were measured. Secondly, the QCM measurements made in this study were *net backscatter rate* measurements, meaning they capture the net effect of both carbon deposition and ion erosion processes. For this reason, although the backscatter yields shown in Fig. 13 show zero net backscatter at 100 V bias, we cannot draw a conclusion over how effectively carbon deposition was reduced. To more conclusively deconvolve deposition and erosion processes at the QCM, future studies might employ a Faraday probe and RPA at the thruster plane to measure the current density and energy levels of the back-launched ion population.

## E. Scaling to Accommodate Higher Power Testing

Scaling a retarding beam catcher to accommodate high thruster powers raises three primary challenges: supplying sufficient plate current, enhancing CEX ion launch-back, and dissipating absorbed power as heat. For the sake of illustration, we can imagine raising the discharge current of our H9 thruster from 15 A (as used in this study) to 150 A (as demonstrated by Su et al.<sup>7</sup>) to achieve higher levels of thrust.

The first consideration is supplying sufficient bias plate current. Increasing thruster current directly increases the incident ion current density ( $j_i$ , in Eq. 16). Doing so by a factor of ten drives up the total plate current required to maintain an active plate bias by a factor of ten. This is illustrated graphically in Fig. 21. We note that a limitation of this prediction is that without test data we cannot infer the Bohm scaling coefficient for collision frequency at this elevated current density. In this study, to hold an active plate bias of 100 V, the plate power supply sourced 4.4 A of current, hence operating at 440 W of power. To hold the same plate bias with a tenfold increase in discharge power, the plate power supply would need to supply 44 A of current, or 4.4 kW of power. This increase in beam catcher power supply current serves as a constraint on facility infrastructure. However, the amount of current necessary to maintain a target plate bias may be reduced by increasing the strength of the beam catcher magnetic field. This is illustrated in Fig. 21, which shows that increasing magnetic field strength (corresponding to a linear increase in coil current) yields a nonlinear reduction of the plate current requirement to hold a fixed bias voltage.

The second consideration is enhancing CEX-driven ion launch-back. At elevated densities of incoming ions, a corresponding increase in neutral density at the beam catcher plate also occurs. As detailed earlier in this section, we believe the neutral density at the plate to be a significant factor in CEX ion launch-back and is a demonstrable problem at the 15 A discharge used in this study. The rate of CEX scales as the product of neutral and ion number densities,<sup>29</sup>  $R_{\text{CEX}} \propto n_n n_i$ . A worst-case approximation for  $n_n$  can be made from number continuity. Assuming monoenergetic ions with  $(V_{\text{acc}} - V_b)$  eV of energy that experience fully diffuse collisions with the plate (i.e. a specular accommodation coefficient of zero), thereby reflecting as neutrals at plate temperature. This yields the scaling relationship

$$n_n = n_i \sqrt{\frac{\pi q(V_{\text{acc}} - V_b)}{4k_B T_p}}, \quad (18)$$

where  $T_p$  represents the plate temperature in Kelvin. For  $V_{\text{acc}} = 300$  V,  $V_b = 150$  V, and  $T_p = 200^\circ$  C,  $R_{\text{CEX}} \propto 54n_i^2$ , and a 10x increase in current density will lead to a 5400x increase in CEX ion generation. In practice, this worst-case scenario should never be realized as the presence of specular collisions at the

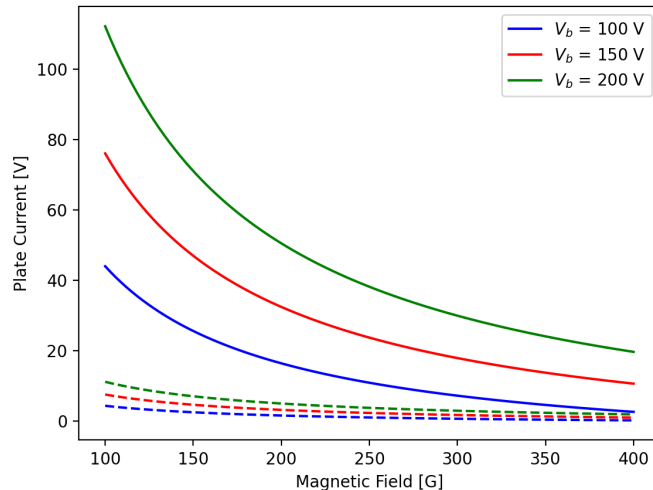


**Figure 21.** Theory-predicted curves for the plate current required to maintain an active bias as a function of magnetic field strength. The solid lines show trends for a 150 A discharge. The dashed lines show trends for the same bias at a 15 A discharge.

bias plate is implied by the increase in background pressure described in Sec. VI. Nevertheless, it demonstrates that ion launch-back is a potentially serious effect at high currents. To address this effect, deliberate redirection of back-launched ions towards alternative capture devices, such as cryopumps, should be made. Facilitating this redirection can be readily achieved by angling the bias plates, though alternative methods such as shaping the electric field vector or curving the magnetic field may also be possible.

A third consideration is thermal management of the beam catcher which, depending on its size, may need to dissipate a significant fraction of the total thruster discharge power. In our example, the total thruster discharge power is raised from 4.5 kW to 45 kW, hence the power dissipated by the plate will rise accordingly. Graphite's ability to withstand elevated temperatures makes it a strong candidate for continued use as a bias plate material. The magnets, therefore, are the limiting material. In our prototype, we used magnet wire insulated with a polyester/polyamideimide coating that has a reported maximum temperature of 200°C. Throughout this study we monitored the temperature of the coils and paused testing when the temperature neared this limit (this limit was low enough that we were unable to identify an equilibrium temperature at this 4.5 kW case). At elevated power levels, temperature mitigations will need to be employed to protect magnet wire insulation material or to prevent the beam catcher from exceeding the Curie temperature if permanent magnets are employed. One potential avenue for hardening an electromagnet to temperature would be to comprise the coil from copper tubes through which a liquid coolant such as water is flowed. This resembles the design of an induction furnace coil, in which the number of turns is highly limited but currents on the order of 900 A can be passed. A theoretical design might consist of 8 turns of 1/4 inch tubing spaced to form a 5 cm wide coil. Powering this coil with 400 A of direct current (representative of an arc welder power supply) would produce an ideal magnetic field strength of 800 G. Additionally, the inclusion of magnetic shunts could enhance magnetic field line concentration, thereby reducing the amount of current required to sustain a given magnetic field strength.

## VII. Conclusion

The problem of backscatter, in which facility material sputtered by an ion beam returns to coat the source, impedes flight qualification testing by obscuring measurements of thruster lifetime. To address this problem, we built and tested a beam catcher designed to electrostatically decelerate ions prior to their striking a graphite plate. An active bias applied to the plate retards incoming ions while a transverse magnetic field suppresses electron current to the plate, thereby enabling large retarding potentials to be achieved. Previous studies confirmed that backscatter reduction can be achieved in this manner, but were

limited in their ability to apply retarding biases and did not evaluate the impact on thruster performance. In this work, we expanded upon previously derived theory, conducted a parametric study to determine the accessible operating biases achievable by a beam catcher, and assessed the beam catcher's impact on thruster performance.

We placed a  $1.3 \times 0.66$  m beam catcher in the far-field plume of a 4.5 kW Hall effect thruster. Placing it in the far-field reduced the plasma density at the plate, enabling us to achieve higher active bias potentials than in previous work,<sup>17</sup> as commensurate with derived theory. We parametrically varied the active bias potential from 0 V to 200 V and magnetic field strengths from 0 G to 200 G. From this, we confirmed that the beam catcher is able to support large plate biases with only minimal impacts on the adjacent plasma. Furthermore, we found that the thruster's far-field plume potential, thrust, and anode current oscillations are not impacted by the beam catcher, even at high retarding biases. We also observed that the plume distribution effectively widens with higher applied biases and attribute this effect to a rise in background pressure as decelerated ions reflect off the beam catcher with lower speeds at higher biases.

We also confirmed that the application of a retarding bias has a direct impact on backscatter rates at the thruster plane. Backscatter rates varied from  $2.91 \mu\text{m}/\text{kHr}$  for an unbiased beam dump to  $-1.99 \mu\text{m}/\text{kHr}$  for a 150 V bias. The presence of negative backscatter rates indicate the onset of an erosion process at high applied biases. We believe that this process is caused by high speed ions undergoing charge exchange with low speed neutrals near the edge of the plate to create low speed ions that are accelerated away from the beam catcher by the plate bias. A limitation of this study is that the net backscatter rates we measured do not provide enough information to separate the impacts of reduced carbon deposition from increased ion erosion at large plate biases.

Ultimately, this work demonstrates that a magnetically assisted retarding beam dump can be used to apply retarding biases in excess of 100 V to a Hall thruster ion beam at representative conditions without affecting thruster operation beyond increasing plume divergence. Furthermore, we showed that the applied bias voltage has a direct impact on backscatter rate, though introduces a new erosion effect by launching ions back at the thruster. Nevertheless, we propose avenues for mitigating this effect and scaling the beam catcher for use with higher power systems. This proof of concept thereby provides a potential path for enabling improved fidelity testing of next-generation propulsion systems.

## Acknowledgments

This work was supported by the Joint Advanced Propulsion Institute, a NASA Space Technology Research Institute, and by the National Science Foundation Graduate Research Fellowship Program. The authors would like to thank Dr. Tate Gill for helpful advice estimating the scaling of charge exchange rates.

## References

- <sup>1</sup>Benjamin Jorns et al. Mechanisms for pole piece erosion in a 6-kw magnetically-shielded hall thruster. In *52nd AIAA/SAE/ASEE Joint Propulsion Conference*, page 4839, 2016.
- <sup>2</sup>Matthew P Byrne et al. Coupling of electrical and pressure facility effects in hall effect thruster testing. *meta*, 5:2, 2006.
- <sup>3</sup>Robert B Lobbia et al. Accelerating 23,000 hours of ground test backscattered carbon on a magnetically shielded hall thruster. In *AIAA Propulsion and Energy 2019 Forum*, page 3898, 2019.
- <sup>4</sup>Jason D Frieman, Hani Kamhawi, Wensheng Huang, Jon Mackey, Drew M Ahern, Peter Y Peterson, James H Gilland, Scott J Hall, Richard R Hofer, Derek Inaba, et al. Wear test of the 12.5-kw advanced electric propulsion system engineering test unit hall thruster. In *AIAA Propulsion and Energy 2020 Forum*, page 3625, 2020.
- <sup>5</sup>Rohit Shastry et al. Status of nasa's evolutionary xenon thruster (next) long-duration test as of 50,000 h and 900 kg throughput. In *International Electric Propulsion Conference (IEPC2013)*, number IEPC-2013-121, 2015.
- <sup>6</sup>James H Gilland, George Williams, Jonathan M Burt, and John Yim. Carbon back sputter modeling for hall thruster testing. In *52nd AIAA/SAE/ASEE Joint Propulsion Conference*, page 4941, 2016.
- <sup>7</sup>Leanne L Su et al. Operation and performance of a magnetically shielded hall thruster at ultrahigh current densities on xenon and krypton. In *AIAA SCITECH 2023 Forum*, page 0842, 2023.
- <sup>8</sup>Mitchell LR Walker et al. Overview of the joint advanced propulsion institute (janus). In *37th International Electric Propulsion Conference*, 2022.
- <sup>9</sup>Jason D Frieman, Hani Kamhawi, George Williams, Wensheng Huang, Daniel A Herman, Peter Y Peterson, James H Gilland, and Richard R Hofer. Long duration wear test of the nasa hermes hall thruster. In *2018 Joint Propulsion Conference*, page 4645, 2018.
- <sup>10</sup>Richard R Hofer, Benjamin A Jorns, James E Polk, Ioannis G Mikellides, and John Steven Snyder. Wear test of a magnetically shielded hall thruster at 3000 seconds specific impulse. In *33rd International Electric Propulsion Conference*, pages 1–24, 2013.

- <sup>11</sup>Ioannis G et al. Mikellides. Assessment of pole erosion in a magnetically shielded hall thruster. In *50th AIAA/ASME/SAE/ASEE Joint Propulsion Conference*, page 3897, 2014.
- <sup>12</sup>Jerold Emhoff and Iain Boyd. Grid erosion modeling of the next ion thruster optics. In *39th AIAA/ASME/SAE/ASEE Joint Propulsion Conference and Exhibit*, page 4868, 2003.
- <sup>13</sup>Graeme T Sabiston and Richard E Wirz. Thrust densification of space electric propulsion systems via volumetrically complex materials. In *AIAA SCITECH 2024 Forum*, page 1136, 2024.
- <sup>14</sup>Jason D Frieman, Scott T King, Mitchell LR Walker, Vadim Khayms, and David King. Role of a conducting vacuum chamber in the hall effect thruster electrical circuit. *Journal of Propulsion and Power*, 30(6):1471–1479, 2014.
- <sup>15</sup>Jonathan A Walker et al. Electrical facility effects on hall-effect-thruster cathode coupling: Discharge oscillations and facility coupling. *Journal of Propulsion and Power*, 32(4):844–855, 2016.
- <sup>16</sup>Seth J Thompson, Jack Garman, Zach C Robertson, John D Williams, William Hurley, Tate Gill, Collin B Whittaker, and Benjamin Jorns. Methods for mitigating backscatter in electric propulsion test facilities i: Beam halter concept and design. In *AIAA SCITECH 2024 Forum*, page 2367, 2024.
- <sup>17</sup>William J Hurley et al. Methods for mitigating backscatter in electric propulsion test facilities ii: Beam halter demonstration during hall thruster testing (upcoming). In *AIAA SciTech 2024 Forum*, 2024.
- <sup>18</sup>Eric A Viges, Benjamin A Jorns, Alec D Gallimore, and JP Sheehan. University of michigan's upgraded large vacuum test facility. In *36th International Electric Propulsion Conference*, pages 1–18, 2019.
- <sup>19</sup>John Williams, Mark Johnson, and Desiree Williams. Differential sputtering behavior of pyrolytic graphite and carbon-carbon composite under xenon bombardment. In *40th AIAA/ASME/SAE/ASEE Joint Propulsion Conference and Exhibit*, page 3788, 2004.
- <sup>20</sup>Dan M Goebel, Ira Katz, and Ioannis G Mikellides. *Fundamentals of electric propulsion*. John Wiley & Sons, 2023.
- <sup>21</sup>Richard R Hofer, Sarah E Cusson, Robert B Lobbia, and Alec D Gallimore. The h9 magnetically shielded hall thruster. In *35th International Electric Propulsion Conference*, pages 2017–232. Electric Rocket Propulsion Soc., 2017.
- <sup>22</sup>Chih-Shun Lu and Owen Lewis. Investigation of film-thickness determination by oscillating quartz resonators with large mass load. *Journal of Applied Physics*, 43(11):4385–4390, 1972.
- <sup>23</sup>Robert B Lobbia and Brian E Beal. Recommended practice for use of langmuir probes in electric propulsion testing. *Journal of Propulsion and Power*, 33(3):566–581, 2017.
- <sup>24</sup>Ville Satopaa, Jeannie Albrecht, David Irwin, and Barath Raghavan. Finding a "kneedle" in a haystack: Detecting knee points in system behavior. In *2011 31st international conference on distributed computing systems workshops*, pages 166–171. IEEE, 2011.
- <sup>25</sup>Kunning G Xu and Mitchell LR Walker. High-power, null-type, inverted pendulum thrust stand. *Review of Scientific Instruments*, 80(5), 2009.
- <sup>26</sup>James E Polk, Anthony Pancotti, Thomas Haag, Scott King, Mitchell Walker, Joseph Blakely, and John Ziemer. Recommended practice for thrust measurement in electric propulsion testing. *Journal of Propulsion and Power*, 33(3):539–555, 2017.
- <sup>27</sup>Edgar Yazid Choueiri. Plasma oscillations in hall thrusters. *Physics of Plasmas*, 8(4):1411–1426, 2001.
- <sup>28</sup>P Baille, J-S Chang, A Claude, RM Hobson, GL Ogram, and AW Yau. Effective collision frequency of electrons in noble gases. *Journal of Physics B: Atomic and Molecular Physics*, 14(9):1485, 1981.
- <sup>29</sup>Walter G Vincenti, Charles H Kruger Jr, and T Teichmann. Introduction to physical gas dynamics, 1966.